

Bulk and surface transformations of Ga₂O₃ nanoparticle catalysts for propane dehydrogenation induced by a H₂ treatment

Castro-Fernández, Pedro; Mance, Deni; Liu, Chong; Abdala, Paula M.; Willinger, Elena; Rossinelli, Aurelio A.; Serykh, Alexander I.; Pidko, Evgeny A.; Copéret, Christophe; Fedorov, Alexey

DOI

[10.1016/j.jcat.2022.02.025](https://doi.org/10.1016/j.jcat.2022.02.025)

Publication date

2022

Document Version

Final published version

Published in

Journal of Catalysis

Citation (APA)

Castro-Fernández, P., Mance, D., Liu, C., Abdala, P. M., Willinger, E., Rossinelli, A. A., Serykh, A. I., Pidko, E. A., Copéret, C., Fedorov, A., & Müller, C. R. (2022). Bulk and surface transformations of Ga₂O₃ nanoparticle catalysts for propane dehydrogenation induced by a H₂ treatment. *Journal of Catalysis*, 408, 155-164. <https://doi.org/10.1016/j.jcat.2022.02.025>

Important note

To cite this publication, please use the final published version (if applicable).
Please check the document version above.

Copyright

Other than for strictly personal use, it is not permitted to download, forward or distribute the text or part of it, without the consent of the author(s) and/or copyright holder(s), unless the work is under an open content license such as Creative Commons.

Takedown policy

Please contact us and provide details if you believe this document breaches copyrights.
We will remove access to the work immediately and investigate your claim.



Bulk and surface transformations of Ga₂O₃ nanoparticle catalysts for propane dehydrogenation induced by a H₂ treatment



Pedro Castro-Fernández^a, Deni Mance^b, Chong Liu^{c,1}, Paula M. Abdala^a, Elena Willinger^a, Aurelio A. Rossinelli^d, Alexander I. Serykh^e, Evgeny A. Pidko^c, Christophe Copéret^b, Alexey Fedorov^{a,*}, Christoph R. Müller^{a,*}

^aLaboratory of Energy Science and Engineering, Department of Mechanical and Process Engineering, ETH Zürich, Switzerland

^bLaboratory of Surface and Interfacial Chemistry, Department of Chemistry and Applied Biosciences, ETH Zürich, Switzerland

^cInorganic Systems Engineering, Department of Chemical Engineering, Delft University of Technology, 2629 HZ Delft, the Netherlands

^dOptical Materials Engineering Laboratory, Department of Mechanical and Process Engineering, ETH Zürich, Switzerland

^eZelinsky Institute of Organic Chemistry, RAS, Moscow, 119991, Russia

ARTICLE INFO

Article history:

Received 17 December 2021

Revised 31 January 2022

Accepted 27 February 2022

Available online 5 March 2022

Keywords:

Propane dehydrogenation

Gallium oxide

Oxygen vacancies

Lewis acidity

Surface reconstruction

ABSTRACT

Three γ/β -Ga₂O₃ nanoparticle catalysts that differ in the relative ratio of γ -Ga₂O₃ to β -Ga₂O₃ were prepared to evaluate the effect of H₂ treatment (500 °C, 2 h) on the coordination environment of bulk and surface Ga sites, Lewis acidity and catalytic activity in propane dehydrogenation (PDH). Independent of the H₂ treatment, the initial PDH activity of the γ/β -Ga₂O₃ catalysts increases with the fraction of the β -Ga₂O₃ phase. This is explained by the presence of weak Lewis acid sites (LAS) in β -Ga₂O₃ while such sites are absent in γ -Ga₂O₃. Treatment with H₂ increases the catalytic activity of all three γ/β -Ga₂O₃ catalysts but for different reasons. For catalysts with higher fractions of β -Ga₂O₃, H₂ treatment increases further the relative abundance of weak LAS, likely by generating coordinatively unsaturated Ga sites (such as tricoordinated Ga sites nearby oxygen vacancies). In contrast, H₂ treatment of a catalyst containing a predominant fraction of γ -Ga₂O₃ phase induces disorder in the sub-surface structure of the nanoparticle, that is, it forms gallium and oxygen vacancies in the bulk and favors migration of gallium, and likely also of oxygen, to the surface. This induces a surface reconstruction that notably increases the fraction of strong LAS (and proportionally decreases the fraction of medium LAS), while creating no weak LAS in γ -Ga₂O₃-H₂. Therefore, the increase in the catalytic activity of H₂-treated γ -Ga₂O₃ is explained by the higher density of surface Ga sites in γ -Ga₂O₃-H₂ relative to calcined γ -Ga₂O₃. H₂-treated catalysts that contain a higher relative amount of weak LAS also feature a higher relative abundance of gallium hydride species associated with a low frequency FTIR band at ca. 1931–1939 cm⁻¹, that is, weak LAS likely give weakly-bound hydrides in β -Ga₂O₃. Our results highlight that weak LAS in unsupported Ga₂O₃ catalysts are more active in PDH than mild or strong LAS.

© 2022 The Author(s). Published by Elsevier Inc. This is an open access article under the CC BY-NC-ND license (<http://creativecommons.org/licenses/by-nc-nd/4.0/>).

1. Introduction

Gallium oxide (gallia) is considered as an alternative material to the industrial CrO_x/Al₂O₃ catalyst (Catofin process) for non-oxidative propane dehydrogenation (PDH). [1,2] A gallia-based catalyst formulation that is close to industrial implementation is PtGa/Al₂O₃ (FCDh process) and it has been argued that Ga₂O₃

may be the active phase in this type of catalysts, while Pt serves merely as a promoter, [3] although counterevidence for Pt-based active sites has also been reported. [4–6] However, the atomic structure of the gallia sites that are most active for PDH has yet to be established. A recent study has suggested that weak Lewis acid sites (LAS) drive PDH activity of β -Ga₂O₃ and, based on DFT calculations, these weak LAS have been ascribed to coordinatively unsaturated (M_{cus}) tricoordinated Ga sites (Ga_{III}) in the vicinity of an oxygen vacancy (V_o). [7] In addition, weak Ga-based LAS have shown to be essential for selective PDH in mixed oxide (Ga, Al)₂O₃ catalysts; [8] in addition, weakly acidic extra-framework Ga-oxo clusters have been proposed to be responsible for the

* Corresponding authors at: Laboratory of Energy Science and Engineering, Department of Mechanical and Process Engineering, ETH Zürich, Switzerland.

E-mail addresses: fedorooal@ethz.ch (A. Fedorov), muelchri@ethz.ch (C.R. Müller).

¹ Present address of Chong Liu: State Key Laboratory of Structural Chemistry, Fujian Institute of Research on the Structure of Matter, Chinese Academy of Sciences, Fuzhou, Fujian 350002, China

alkane dehydrogenation activity of Ga-modified high-silica zeolites. [9,10]

H₂ pre-treatment of poorly reducible oxides such as Al₂O₃, TiO₂, ZrO₂ or W₂O₃ was suggested to generate M_{cus} metal sites in those materials and yield PDH active catalysts. [11–17] While H₂ pre-treatment may generate surface V_o sites in the stated oxides (and thereby produces M_{cus} sites), an alternative scenario that can proceed during H₂ treatment is surface reconstruction. More specifically, oxygen can diffuse from the bulk towards the surface, leading to an increased density of V_o sites in the bulk and a reduced number of oxygen vacancies at the surface, and hence also a decreased number of M_{cus} sites. [18,19]

In view of these different scenarios, the aim of this work is to assess the effect of H₂ treatment (500 °C, 2 h) on the surface and bulk sites of three gallia nanoparticle (NP) PDH catalysts. Overall, the catalytic performance of the gallia catalysts may depend on the extent of the surface reduction, which is likely to influence their Lewis acidity properties. The catalysts contain varying ratios of γ/β gallia phases, as determined by X-ray diffraction (XRD) and pair distribution function (PDF) analyses. Ultraviolet–visible spectroscopy (UV–Vis) and dynamic nuclear polarization surface enhanced NMR spectroscopy (DNP SENS) [20,21] using ¹⁵N pyridine as a probe molecule indicate that H₂ treatment generates V_o sites (surface and bulk) in a β-rich Ga₂O₃ catalyst and forms Ga_{cus} (Ga_{III}) surface sites leading to an increased relative fraction of weak LAS and in turn a higher PDH activity of the H₂-treated γ/β-Ga₂O₃ catalysts. Interestingly, H₂ treatment of γ-phase Ga₂O₃ NPs creates bulk V_o sites, giving rise to a disordered bulk structure and a surface reconstruction. This reconstructed surface has a higher density of Ga sites, which may explain the increased PDH activity of H₂-treated γ-phase Ga₂O₃. However, weak LAS are detected neither in the calcined nor the H₂-treated γ-rich Ga₂O₃ materials, and this correlates with a lower PDH activity of these catalysts relative to Ga₂O₃ NPs rich in the β-gallia phase (calcined or H₂-treated).

2. Experimental details

2.1. Synthesis

Nanocrystalline γ-Ga₂O₃ nanoparticles (NPs) were synthesized by an established colloidal approach using gallium acetylacetonate and oleylamine. [22] Specifically, Ga(acac)₃ (2 g, 5.4 mmol, 99.99+%, Strem Chemicals) and 40 mL of C₁₈H₃₅NH₂ (≥98%, Sigma-Aldrich) were stirred at 90 °C for 1 h under dynamic vacuum (ca. 10⁻¹ mbar) in a 100 mL three-neck, round-bottom flask equipped with a reflux condenser, thermocouple and connected to a Schlenk line. This was followed by heating to 200, 250 or 300 °C (3 °C min⁻¹ under N₂ flow and stirring) for 7, 12 or 16 h, respectively. The reaction mixtures were subsequently cooled down to room temperature, dissolved in a 3:1 mixture (volume ratio) of toluene and ethanol (Sigma-Aldrich; ≥99.5% and ≥99.8%, respectively, ca. 35 mL) and centrifuged at 6500 rpm. The precipitate was redispersed in a toluene-ethanol mixture and the centrifugation-redispersion step was repeated four times. The precipitated gel (ca. 25% yield based on thermogravimetric analysis) was dispersed in toluene (ca. 20 mL) and the resulting solution was dried overnight at 110 °C, yielding oleylamine-capped Ga₂O₃ NPs as a powder. Calcination of the as-synthesized gallia NPs in a muffle furnace at 600 °C (3 °C min⁻¹, 2 h) gave calcined materials denoted Ga₂O₃₍₂₀₀₎, Ga₂O₃₍₂₅₀₎ and Ga₂O₃₍₃₀₀₎, with the respective synthesis temperature indicated by the subscript in parenthesis. The reductive treatment of the calcined gallia nanoparticles (ca. 150 mg) was performed in a fixed-bed quartz reactor (13 mm OD) under H₂ at 500 °C (10 °C min⁻¹, 50 mL min⁻¹, 2 h). This reductive treatment gave materials denoted as Ga₂O₃₍₂₀₀₎-H₂, Ga₂O₃₍₂₅₀₎-H₂ and

Ga₂O₃₍₃₀₀₎-H₂. A β-Ga₂O₃₍₇₅₀₎ reference was obtained by calcining Ga₂O₃₍₂₀₀₎ at 750 °C for 2 h. The structures of β-Ga₂O₃₍₇₅₀₎ and Ga₂O₃₍₂₀₀₎ have been described by us previously. [23]

2.2. Methods

Details of the fixed bed catalytic tests for PDH, XRD and PDF analyses, high-angle annular dark field scanning electron microscopy (HAADF-STEM), electron energy loss spectroscopy (EELS), UV–Vis, Ga K-edge X-ray absorption spectroscopy (XAS), ¹⁵N DNP SENS, diffuse reflectance infrared Fourier transform spectroscopy (DRIFTS), inductively coupled plasma - optical emission spectrometry (ICP-OES) and N₂ physisorption data are reported in the [Supporting Information](#).

3. Results

3.1. Materials

Nanocrystalline gallia nanoparticles were obtained by adjusting the synthesis temperature and time at 200, 250 or 300 °C for 7, 12 or 16 h, respectively (Fig. 1A and Figure S1). Calcination in air at 600 °C yielded materials denoted as Ga₂O₃₍₂₀₀₎, Ga₂O₃₍₂₅₀₎ and Ga₂O₃₍₃₀₀₎. Treatment of these materials at 500 °C in a flow of pure H₂ (50 mL min⁻¹, 2 h) gave Ga₂O₃₍₂₀₀₎-H₂, Ga₂O₃₍₂₅₀₎-H₂ and Ga₂O₃₍₃₀₀₎-H₂ (Fig. 1A). H₂ treatment induced a color change from white (calcined Ga₂O₃ nanoparticles) to pale yellow (Figure S2), consistent with their UV–Vis spectra (Figure S3, *vide infra*). When exposed to air, the color of the H₂-treated gallia NPs remained unchanged for ca. four weeks and after this time, the color gradually changed back to white, within ca. six weeks. Because of this relative stability of the Ga₂O₃-H₂ NPs in air, we have performed their characterization in an air atmosphere (unless specified otherwise), but always within 48 h after their first exposure to air.

3.2. Morphology, surface area, Ga content

Table S5 summarizes (i) the particle size distribution (PSD) of the as-synthesized colloidal gallia materials (obtained from TEM data, Figure S4), as well as (ii) the specific surface areas (S_{BET}) and (iii) the Ga wt% content (ICP-OES) of the calcined and H₂-treated nanoparticles. The average sizes of the colloidal gallia nanoparticles, as determined by TEM analysis, are 2.5(6), 4.7(7) and 5.6(8) nm for Ga₂O₃₍₂₀₀₎, Ga₂O₃₍₂₅₀₎ and Ga₂O₃₍₃₀₀₎, respectively, i.e. higher synthesis temperatures and longer holding times lead to a larger particle size. Brunauer-Emmett-Teller (BET) analysis of the N₂ physisorption data shows that the surface area of calcined Ga₂O₃₍₃₀₀₎ is 159 m² g⁻¹, which is higher than that of Ga₂O₃₍₂₅₀₎ and Ga₂O₃₍₂₀₀₎ (122 and 98 m² g⁻¹, respectively). Comparison of the average particle sizes with the respective BET surface areas suggests that calcination-induced agglomeration is highest in Ga₂O₃₍₂₀₀₎ and lowest in Ga₂O₃₍₃₀₀₎. H₂ treatment leads to a decrease in surface area, i.e. the S_{BET} of Ga₂O₃₍₂₀₀₎-H₂, Ga₂O₃₍₂₅₀₎-H₂ and Ga₂O₃₍₃₀₀₎-H₂ are 72, 87 and 101 m² g⁻¹, i.e. a decrease of, respectively, ca. 27%, 29% and 37% after H₂ treatment. The gallium content (Ga wt%), determined by ICP-OES, shows very similar values and ranges between 68 and 70% for all of the six materials studied here (calcined and H₂-treated, Table S5).

3.3. UV–Vis

The band gap energies of the prepared materials are determined by Tauc plots of the UV–Vis spectra (Figure S5 and S3, respectively). [24,25] Ga₂O₃₍₂₀₀₎, Ga₂O₃₍₂₅₀₎ and Ga₂O₃₍₃₀₀₎ show similar band gap energies of 4.1, 4.3 and 4.2 eV, respectively (Table S5).

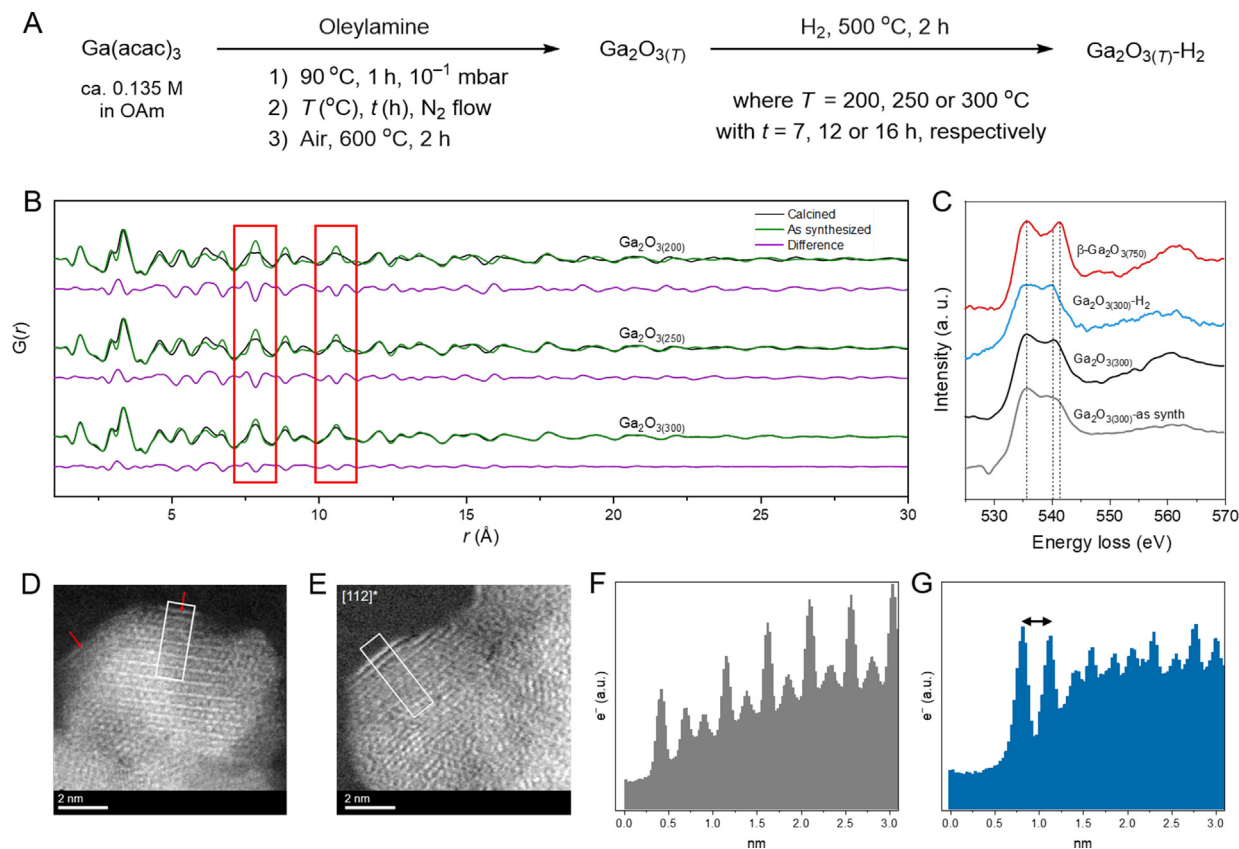


Fig. 1. A) Synthesis of the calcined and H_2 -treated Ga_2O_3 -based materials. Characterization of the structure of the Ga_2O_3 NPs: B) Synchrotron-based PDF ($G(r)$) analysis; the red boxes highlight features (broadened and split peaks) that indicate the presence of $\beta\text{-Ga}_2\text{O}_3$. [7,23] C) O K-edge EELS spectra of $\text{Ga}_2\text{O}_3(300)$ (as-synthesized, calcined and H_2 -treated) along with the $\beta\text{-Ga}_2\text{O}_3(750)$ reference; a zoom into the pre-edge features (at ca. 530 eV) of these materials is given in Figure S13. D) HAADF-STEM image of $\text{Ga}_2\text{O}_3(300)$ with red arrows pointing at particle edges. E) HAADF-STEM image of $\text{Ga}_2\text{O}_3(300)\text{-H}_2$. Panels F and G) show HAADF STEM line intensity profiles along the [111] plane based on the areas defined by the white rectangles in images D) and E), respectively. The double-headed arrow in G) indicates the distance between the two outermost atomic layers in E). Note that the synchrotron-based PDF data of as-synthesized and calcined $\text{Ga}_2\text{O}_3(200)$ have been reported by us previously, [7] and it is reproduced here for the sake of comparison and completeness. (For interpretation of the references to color in this figure legend, the reader is referred to the web version of this article.)

These values are close to the reported band gap in $\gamma\text{-Ga}_2\text{O}_3$ quantum dots (4.5 eV), [26] and are below the reported band gap of $\beta\text{-Ga}_2\text{O}_3$ (4.8–4.9 eV). [27] The H_2 -treated Ga_2O_3 NPs, which were exposed to atmospheric air before measurement, display a red shift of UV-Vis absorption relative to calcined Ga_2O_3 NPs (Figure S3), and an absorption tail that extends into the visible region likely relates to the sub-bandgap absorption by the deep defect states (V_o sites). [28–30] Consequently, the H_2 -treated Ga_2O_3 NPs have significantly lower band gaps, viz. 3.4, 3.9 and 3.9 eV for $\text{Ga}_2\text{O}_3(200)\text{-H}_2$, $\text{Ga}_2\text{O}_3(250)\text{-H}_2$ and $\text{Ga}_2\text{O}_3(300)\text{-H}_2$, respectively (Figure S5, Table S5), consistent with formation of discrete intra-band gap energy states in the reduced materials due to V_o sites. [31,32]

3.4. XRD and PDF analyses

Diffractograms of the three as-synthesized Ga_2O_3 NPs (before calcination) show broad peaks that are attributed to the metastable $\gamma\text{-Ga}_2\text{O}_3$ phase (Figure S6). The patterns of the calcined gallia NPs (black) also display broad peaks due to $\gamma\text{-Ga}_2\text{O}_3$ (Figure S7). [33] However, the diffractogram of $\text{Ga}_2\text{O}_3(200)$ shows subtle features of the $\beta\text{-Ga}_2\text{O}_3$ phase at 2θ of ca. 32, 46, 48 and 57° (red asterisks in Figure S7), indicating a partial phase transformation from $\gamma\text{-Ga}_2\text{O}_3$ to $\beta\text{-Ga}_2\text{O}_3$ after calcination at 600°C . The irreversible $\gamma \rightarrow \beta$ (bulk) transformation has been reported to take place at temperatures above 600°C . [33] However, we have also observed previously that already at temperatures close to 300°C the local structure (<1 nm range) of $\text{Ga}_2\text{O}_3(200)$ undergoes a transformation

leading to the formation of small $\beta\text{-Ga}_2\text{O}_3$ domains at such temperatures. [23]

Thus, the XRD results suggest that the conditions of the colloidal synthesis (temperature and reaction duration) influence the extent to which $\gamma\text{-Ga}_2\text{O}_3$ transforms into $\beta\text{-Ga}_2\text{O}_3$ during calcination, i.e. $\text{Ga}_2\text{O}_3(200) > \text{Ga}_2\text{O}_3(250) > \text{Ga}_2\text{O}_3(300)$. This is possibly due to the difference in the particle sizes of the as-synthesized $\gamma\text{-Ga}_2\text{O}_3$ NPs as observed by TEM (Table S5). H_2 treatment does not lead to any notable changes in the diffractograms (Figure S7, blue traces).

Complementary insight into the nanocrystalline structure of the calcined and/or H_2 -treated materials was obtained using PDF analysis (synchrotron-based data). [23] The PDF of the as-synthesized materials is similar to previous reports on $\gamma\text{-Ga}_2\text{O}_3$ that have shown that this phase exhibits an intrinsic high degree of disorder (Fig. 1B). [23] The peak at ca. 1.9 Å is due to Ga–O pairs (Table S2) and its position is determined by the average Ga–O interatomic distances, that depend on the relative abundances (and asymmetry) of the GaO_4 and GaO_6 polyhedra in the gallia phases, while the peaks in the region 2.7–4.0 Å are dominated by Ga–Ga pairs of the GaO_4 and GaO_6 polyhedra.

Despite the initial crystalline structure of the NPs is similar among the three studied as-synthesized catalysts (i.e. $\gamma\text{-Ga}_2\text{O}_3$), after calcination these materials undergo changes to a different extent due to a partial $\gamma \rightarrow \beta$ transformation at 600°C (in line with XRD observations). This can be seen in Fig. 1B, which plots difference curves (d-PDF), i.e. the PDF data of the as-synthesized materials is subtracted from that of the respective calcined

nanoparticles. The degree of $\gamma \rightarrow \beta$ transformation (i.e. higher β -phase content) follows the trend: $\text{Ga}_2\text{O}_3(300) < \text{Ga}_2\text{O}_3(250) < \text{Ga}_2\text{O}_3(200)$. This trend is also confirmed by the characteristic peak splitting at ca. 7.9 Å and 10.5 Å, linked to the emergence of β - Ga_2O_3 in the structure (marked by red rectangles in Fig. 1B). [7,23] To quantify the extent of phase transformation for each catalyst during calcination, the mid-range of the PDF data (5–17 Å which contains information on the average structure of the materials) was fitted using γ - and β - Ga_2O_3 models. [34,35] The fitting results (Figure S8) show atomic percentages of β - Ga_2O_3 of ca. 40%, 30% and 20% for $\text{Ga}_2\text{O}_3(200)$, $\text{Ga}_2\text{O}_3(250)$ and $\text{Ga}_2\text{O}_3(300)$, respectively. The average crystallite sizes were also obtained from such fittings. We observe increases in the crystallite sizes from ca. 2.4 to 3 nm in $\text{Ga}_2\text{O}_3(300)$, and from ca. 2.8 to 3.4 nm in $\text{Ga}_2\text{O}_3(250)$ and $\text{Ga}_2\text{O}_3(200)$.

An additional (laboratory-based) PDF analysis was carried out to identify possible structural differences between the calcined and H_2 -treated materials (Figures S9, S10 and Table S2). The PDF analysis shows that there are no considerable structural changes during H_2 treatment, yet we can observe slight variations in the range of ca. 3.1–3.5 Å that are possibly related to an increased degree of disorder after H_2 treatment.

3.5. Ga K-edge XAS

The coordination and the local structure of Ga in calcined and H_2 -treated Ga_2O_3 nanoparticles were probed by Ga K-edge XAS that originates from the $1s \rightarrow 4p$ transition and is sensitive to the geometry of the Ga–O coordination. The features at ca. 10376 eV and 10379 eV in the X-ray absorption near edge structure (XANES) spectra of the Ga_2O_3 NPs studied have been attributed to four- (Ga_{IV}) and six-coordinated (Ga_{VI}) sites, respectively. [36] The XANES spectra of the calcined (black) and H_2 -treated (blue) materials are presented in Figure S11. The XANES features, i.e. the positions of the Ga_{IV} and Ga_{VI} features are similar in the studied materials. $\text{Ga}_2\text{O}_3(250)$ has the highest intensity, compared to $\text{Ga}_2\text{O}_3(200)$ and $\text{Ga}_2\text{O}_3(300)$, particularly for the feature at 10379 eV, possibly related to a higher Ga–O coordination number in this material. After H_2 treatment we observe a systematic decrease in the white line intensity in all of the H_2 -treated materials compared to the calcined materials, suggesting a change in the local structure of Ga, in line with results of EXAFS and EELS analyses (*vide infra*). The decrease of the white line intensity in the XANES spectra of the H_2 -treated materials can be related to a decrease in the Ga–O coordination number as determined by EXAFS (*vide infra*) likely due to a more defective structure.

Figure S11 presents non-phase-corrected Fourier transform (FT) plots of the extended X-ray absorption fine structure (EXAFS) data. EXAFS fittings of the calcined and H_2 -treated materials are presented in Figure S12 and fitting results are reported in Table S3. We fitted the FT data between 1 and 3 Å using a simplified model composed of one Ga–O and two Ga–Ga paths. It should be noted that these fits represent only an average structure since a mixture of γ and β phases is present in the studied materials and hence a distribution of Ga–O and Ga–Ga distances occur in the fitted range. The average coordination numbers (CN) of the Ga–O and Ga–Ga shells show a slight decrease in the H_2 -treated catalysts which suggests that H_2 treatment induces disorder in the local structure for all catalysts (Figure S12, Table S3).

3.6. EELS

Electron energy loss spectroscopy at the O K-edge was used to characterize $\text{Ga}_2\text{O}_3(300)$ (as synthesized and calcined) and $\text{Ga}_2\text{O}_3(300)\text{-H}_2$. We have chosen $\text{Ga}_2\text{O}_3(300)$ for EELS analysis because it shows the highest content of the γ - Ga_2O_3 phase, which

makes the interpretation of structural transformations induced by H_2 treatment easier as it is not influenced notably by the phase transition ($\gamma \rightarrow \beta$). For benchmarking, the β - $\text{Ga}_2\text{O}_3(750)$ reference was analyzed as well. The EELS spectra in Fig. 1C show two peaks owing to the hybridization of the O 2p and Ga 4s states (at ca. 536 eV) and O 2p and Ga 4p states (at ca. 541 eV). The broad feature at ca. 560 eV is attributed to the multiple-scattering of electrons. [37] The peak at ca. 536 eV has a similar shape and intensity for all materials except for $\text{Ga}_2\text{O}_3(300)\text{-H}_2$ for which a lower intensity and peak broadening is observed. The peak at ca. 541 eV is more well-defined in calcined $\text{Ga}_2\text{O}_3(300)$ relative to as-synthesized $\text{Ga}_2\text{O}_3(300)$, and it also shifts to ca. 540.5 eV in $\text{Ga}_2\text{O}_3(300)$. This peak shifts further to ca. 539.9 eV in $\text{Ga}_2\text{O}_3(300)\text{-H}_2$. In contrast, this peak is found at higher energies of ca. 541.5 eV in β - $\text{Ga}_2\text{O}_3(750)$. In general, $\text{Ga}_2\text{O}_3(300)\text{-H}_2$ features broader and lower intensity peaks at ca. 536 and 540 eV relative to the other three materials studied here. Noteworthy, $\text{Ga}_2\text{O}_3(300)\text{-H}_2$ contains a pre-edge feature at ca. 530 eV that is not found in any of the other three materials (Fig. 1C, Figure S13). Such a pre-edge feature might be due to new energy states in the band gap (i.e. V_o sites) that are created during the H_2 treatment. [38]

Lastly, we compared the EELS spectra of $\text{Ga}_2\text{O}_3(300)\text{-H}_2$ exposed to air for either less than two days or three months. The material that has been exposed to air for 3 months features an EELS spectrum that is very similar to that of $\text{Ga}_2\text{O}_3(300)$, consistent with a re-oxidation of the material during the prolonged exposure to air (Figure S14).

3.7. HAADF-STEM

We have reported previously, using HAADF-STEM analysis, that $\text{Ga}_2\text{O}_3(200)$ NPs contain in the surface layers a higher fraction of Ga sites in octahedral crystallographic positions compared to bulk sites. In addition, small crystallites of the β - Ga_2O_3 phase have been observed previously by HAADF-STEM in $\text{Ga}_2\text{O}_3(200)$. [23] Here, we additionally characterize $\text{Ga}_2\text{O}_3(300)$ and $\text{Ga}_2\text{O}_3(300)\text{-H}_2$ by HAADF-STEM imaging because these materials show the lowest content of the β - Ga_2O_3 phase, as observed by XRD and PDF, and because $\text{Ga}_2\text{O}_3(300)\text{-H}_2$ exhibits a notable disorder, relative to $\text{Ga}_2\text{O}_3(300)$, (according to EXAFS analysis). [23] HAADF-STEM imaging of $\text{Ga}_2\text{O}_3(300)$ reveals particles with well-defined edges and a crystalline core (Fig. 1D). In contrast, $\text{Ga}_2\text{O}_3(300)\text{-H}_2$ features a more disordered core (Fig. 1E). Interestingly, the edge regions become more ordered during H_2 treatment. Plotting the intensities of the atomic columns along the [111] planes reveal a higher occupancy of Ga_{VI} positions in the surface layers of $\text{Ga}_2\text{O}_3(300)\text{-H}_2$ as compared to $\text{Ga}_2\text{O}_3(300)$. In contrast, there is a decrease in the site occupancy in subsurface layers of $\text{Ga}_2\text{O}_3(300)\text{-H}_2$ compared to $\text{Ga}_2\text{O}_3(300)$ (Fig. 1F–G). These data show that the surface layers in $\text{Ga}_2\text{O}_3(300)\text{-H}_2$ become denser, and therefore more ordered relative to $\text{Ga}_2\text{O}_3(300)$.

3.8. Dissociation of H_2

The heterolytic dissociation of hydrogen over Ga–O bonds yielding gallium hydrides and hydroxyl groups was studied by DRIFTS. Here, the calcined NPs were dehydroxylated overnight in an in situ cell (Praying Mantis, Harrick) at 550 °C at ca. 10^{-4} mbar (measured at the cell outlet). Subsequently, pure H_2 was flowed through the cell for 2 h (15 mL min^{-1}) at 500 °C and IR spectra were collected. The cell was evacuated at 550 °C at ca. 10^{-4} mbar for ca. 2 h and the spectrum of the outgassed specimen acquired.

Fig. 2 presents parts of the full IR spectra focusing on the regions of Ga–OH ($3800\text{--}3200 \text{ cm}^{-1}$) and Ga–H vibrations ($2100\text{--}1900 \text{ cm}^{-1}$). [39,40] For dehydroxylated Ga_2O_3 NPs, the region of the Ga hydroxyl groups (ca. $3800\text{--}3500 \text{ cm}^{-1}$) contains three main

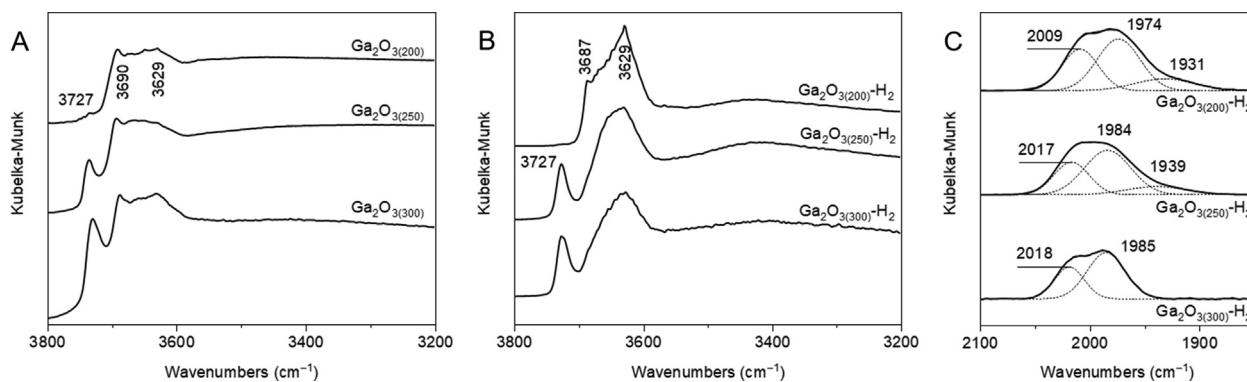


Fig. 2. FTIR spectra of the Ga hydroxyls region (3800–3400 cm^{-1}) after evacuation at 550 $^{\circ}\text{C}$ for 2 h (A) and subsequent H_2 treatment at 500 $^{\circ}\text{C}$ for 2 h (B). (C) Fitted FTIR spectra of the Ga hydride region after evacuation at 550 $^{\circ}\text{C}$ and H_2 adsorption at 500 $^{\circ}\text{C}$.

bands at ca. 3727, 3690 and 3629 cm^{-1} (Fig. 2A). Interestingly, the intensity of the band at ca. 3727 cm^{-1} increases in the following order: $\text{Ga}_2\text{O}_3(200) < \text{Ga}_2\text{O}_3(250) < \text{Ga}_2\text{O}_3(300)$. Bands at ca. 3690 and 3629 cm^{-1} show similar intensities in all of the three materials studied. The band at ca. 3727 cm^{-1} has been related to terminal OH groups bonded to tetrahedral Ga surface sites. [41,42] H_2 treatment does not lead to major changes of this band for $\text{Ga}_2\text{O}_3(300)\text{-H}_2$ and $\text{Ga}_2\text{O}_3(250)\text{-H}_2$, while the band disappears almost entirely in $\text{Ga}_2\text{O}_3(200)\text{-H}_2$. According to the literature, the sharp Ga–OH band at ca. 3727 cm^{-1} has been observed mainly in $\gamma\text{-Ga}_2\text{O}_3$ spinel materials and related to the presence of cation vacancies in nonstoichiometric spinels. [41] In contrast, broader bands at lower frequencies have been ascribed to hydroxyls bonded to Ga sites located on terraces. [43] After H_2 treatment (Fig. 2B), the band at ca. 3687 cm^{-1} largely disappears in all of the materials, except for $\text{Ga}_2\text{O}_3(200)\text{-H}_2$.

After H_2 treatment at 500 $^{\circ}\text{C}$, Gaussian fittings of the intensity-normalized Ga–H bands resolve three bands at ca. 2009, 1974 and 1931 cm^{-1} for $\text{Ga}_2\text{O}_3(200)\text{-H}_2$, at ca. 2017, 1984 and 1939 cm^{-1} for $\text{Ga}_2\text{O}_3(250)\text{-H}_2$; but only two bands at ca. 2018 and 1985 cm^{-1} for $\text{Ga}_2\text{O}_3(300)\text{-H}_2$. While the fitted area distributions for each band are similar for $\text{Ga}_2\text{O}_3(200)\text{-H}_2$ and $\text{Ga}_2\text{O}_3(250)\text{-H}_2$, the respective frequencies of the bands are higher for $\text{Ga}_2\text{O}_3(250)\text{-H}_2$. For $\text{Ga}_2\text{O}_3(300)\text{-H}_2$, the two higher frequency bands appear at similar wavenumbers as in $\text{Ga}_2\text{O}_3(250)\text{-H}_2$, while the band at ca. 1939 cm^{-1} is not present. Note that a desorption step at 550 $^{\circ}\text{C}$ for 2 h led to a complete disappearance of the hydride bands and restored the OH signatures of the initial dehydroxylated materials.

The high and low frequency Ga–H bands centered at ca. 2020 and 1980 cm^{-1} have been attributed, respectively, to $\text{Ga}_{\text{IV}}\text{-H}$ and $\text{Ga}_{\text{VI}}\text{-H}$ sites; a band at a higher vibration frequency is associated with a stronger Ga–H bond. [39,44,45] Therefore, the bands located at ca. 1939 and 1931 cm^{-1} in $\text{Ga}_2\text{O}_3(250)\text{-H}_2$ and $\text{Ga}_2\text{O}_3(200)\text{-H}_2$ respectively suggest the presence of weaker Ga–H moieties in these two materials while they are absent in $\text{Ga}_2\text{O}_3(300)\text{-H}_2$.

3.9. DFT modelling

Using DFT models of dehydroxylated $\beta\text{-Ga}_2\text{O}_3$ surfaces described by us previously, [7] we have evaluated if a more detailed assignment of Ga–H bands can be made. Ga hydrides were simulated as $\text{Ga}_{\text{V}}\text{-H}$ and $\text{Ga}_{\text{III}}\text{-H}$ sites, both isolated and interacting with a vicinal OH group. In addition, the effect of the presence of V_o surface sites on the vibration frequency was explored. The structural models along with the respective hydrogen binding energies and Ga–H bond vibrations obtained from our DFT calculations are displayed in Figure S15. Results show that the presence of a vicinal V_o site induces a decrease in the Ga–H stretching vibration frequency, that is, $\text{Ga}_{\text{V}}\text{-H}$ sites feature higher stretching

frequencies than $\text{Ga}_{\text{III}}\text{-H}$ sites. In the vicinity of hydroxyl groups, both $\text{Ga}_{\text{V}}\text{-H}$ and $\text{Ga}_{\text{III}}\text{-H}$ frequencies decrease. Similarly to the previous DFT studies of Ga hydrides on $\beta\text{-Ga}_2\text{O}_3$, [46] we observe a linear correlation between Ga–H bond distances and FTIR wavenumbers, that is, shorter Ga–H bond distances correspond to higher wavenumbers (Figure S16).

3.10. ^{15}N DNP SENS

The distribution of surface acid sites in the prepared NPs was studied by ^{15}N DNP SENS using ^{15}N -labelled pyridine (Py) as the probe molecule. [47,48] After the dehydroxylation of calcined and H_2 -treated gallia NPs at 500 $^{\circ}\text{C}$ under ca. 10^{-5} mbar for 2 h, the materials were contacted with Py vapor at room temperature, followed by desorption at 100 $^{\circ}\text{C}$ for 15 min (ca. 10^{-5} mbar). The materials obtained were stored in a glovebox and handled without any contact to air. Py bound to strong, medium and weak Ga LAS resonates at ca. 235–240, 255–265 and 275–285 ppm, respectively (the chemical shift of bound Py depends on the desorption temperature, i.e. on the surface coverage of Py). [49,50] However, peaks due to Py on weak LAS and weak BAS overlap (ca. 280–285 ppm). $\text{Ga}_2\text{O}_3(200)$ and $\text{Ga}_2\text{O}_3(250)$ feature shoulders at ca. 277 ppm (7%) and 283 ppm (4%) that are assigned to Py bound to weak LAS (Fig. 3). [7] $\text{Ga}_2\text{O}_3(300)$ contains no weak LAS. According to the fits, the fraction of Py bound to medium LAS comprises 57, 72 and 70% in $\text{Ga}_2\text{O}_3(200)$, $\text{Ga}_2\text{O}_3(250)$ and $\text{Ga}_2\text{O}_3(300)$, respectively while Py bound to strong LAS comprises 36, 24 and 30% in $\text{Ga}_2\text{O}_3(200)$, $\text{Ga}_2\text{O}_3(250)$ and $\text{Ga}_2\text{O}_3(300)$, respectively. Upon H_2 treatment, the peak due to Py bound to weak LAS increases strongly in $\text{Ga}_2\text{O}_3(200)\text{-H}_2$, i.e. to 27%, but only modestly in $\text{Ga}_2\text{O}_3(250)\text{-H}_2$, i.e. to 6%. On the other hand, H_2 treatment of $\text{Ga}_2\text{O}_3(300)$, does not lead to the formation of weak LAS in $\text{Ga}_2\text{O}_3(300)\text{-H}_2$. Furthermore, the reductive treatment does not seem to affect the fraction of Py bound to medium LAS in $\text{Ga}_2\text{O}_3(200)$ and $\text{Ga}_2\text{O}_3(250)$, i.e. the fitted intensity of Py on medium LAS remains at ca. 55 and 70% in, respectively, $\text{Ga}_2\text{O}_3(200)\text{-H}_2$ and $\text{Ga}_2\text{O}_3(250)\text{-H}_2$, but the fraction of Py bound to medium LAS decreases to 43% in $\text{Ga}_2\text{O}_3(300)\text{-H}_2$. In addition, the fraction of Py bound to strong LAS decreases strongly in $\text{Ga}_2\text{O}_3(200)\text{-H}_2$, i.e. to 18%, is unaffected in $\text{Ga}_2\text{O}_3(250)\text{-H}_2$ (24%) and increases strongly in $\text{Ga}_2\text{O}_3(300)\text{-H}_2$, to 57%.

3.11. Catalytic Performance

Catalytic tests for PDH have been performed at 550 $^{\circ}\text{C}$ and GC data have been collected between 4 and 104 min of time on stream (TOS) (Fig. 4A, Table S4). Among the calcined catalysts, $\text{Ga}_2\text{O}_3(200)$ and $\text{Ga}_2\text{O}_3(250)$ show the highest initial surface area-normalized (areal) activity, followed by $\text{Ga}_2\text{O}_3(300)$ (after 4 min TOS, the activity is 139, 138 and 112 $\mu\text{mol C}_3\text{H}_6 \text{ m}^{-2} \text{ h}^{-1}$ for $\text{Ga}_2\text{O}_3(200)$, $\text{Ga}_2\text{O}_3(250)$

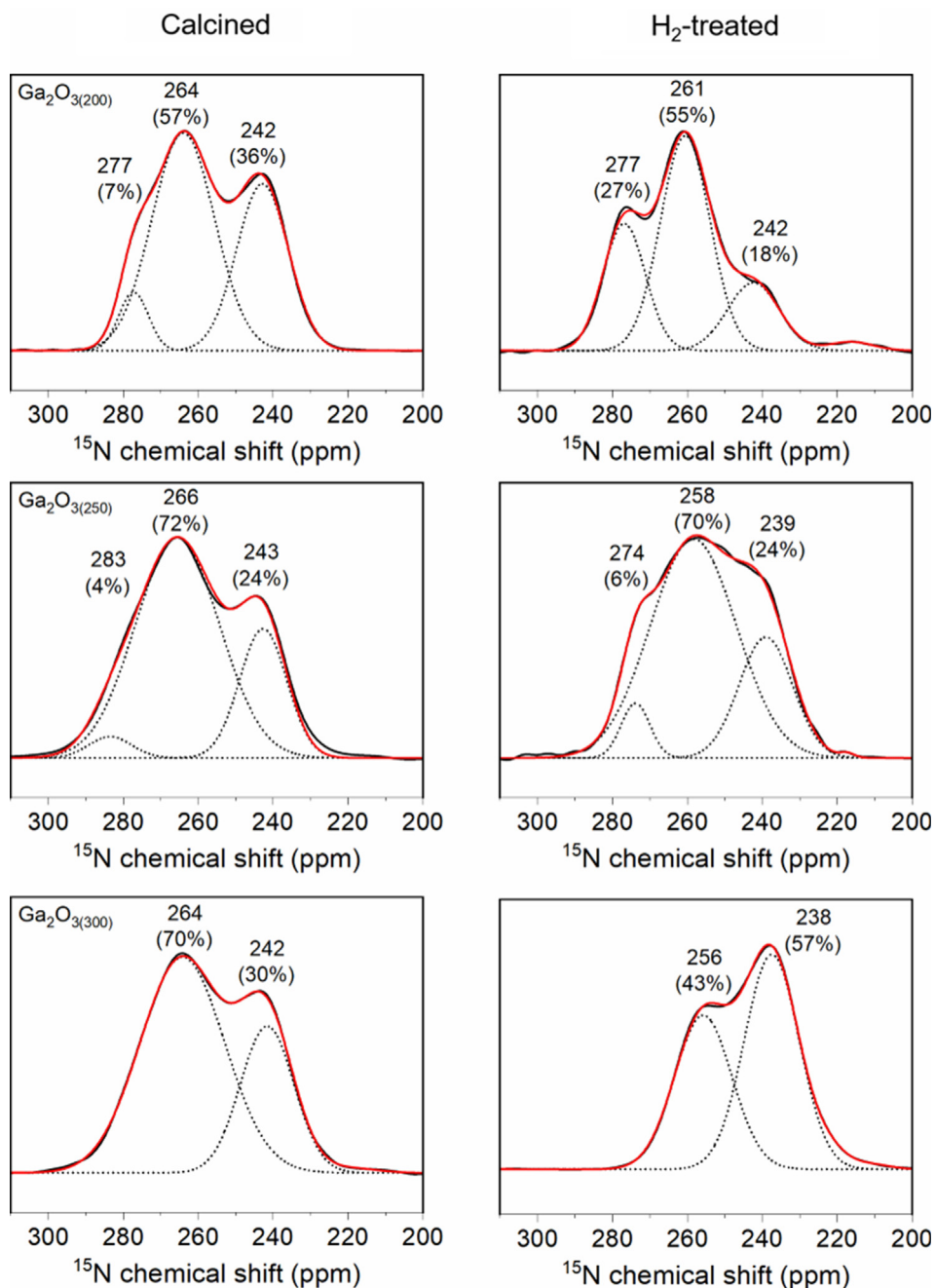


Fig. 3. ^{15}N DNP SENS spectra obtained after the desorption of Py at $100\text{ }^\circ\text{C}$ (10^{-5} mbar, 15 min). Captions show the chemical shift and the relative percentage (in parenthesis) of the total peak area obtained by Gaussian fittings. Note that the spectrum of Py on $\text{Ga}_2\text{O}_3(200)$ has been reported by us previously, [7] and is reproduced here for the sake of comparison and completeness.

and $\text{Ga}_2\text{O}_3(300)$, respectively), with similar initial propane conversions (4 min TOS) within ca. 30–33% (Table S4). After 104 min TOS the surface area-normalized catalytic activity has declined by ca. 3.9, 2.9 and 3.3 times for $\text{Ga}_2\text{O}_3(200)$, $\text{Ga}_2\text{O}_3(250)$ and $\text{Ga}_2\text{O}_3(300)$, respectively. The H_2 -treated catalysts have been prepared in situ prior to the catalytic test ($500\text{ }^\circ\text{C}$, 2 h, 40 mL min^{-1}) followed by a 15 min purge with N_2 (40 mL min^{-1}) to remove chemisorbed H_2 from the surface. The initial areal activity of $\text{Ga}_2\text{O}_3(200)\text{-H}_2$, $\text{Ga}_2\text{O}_3(250)\text{-H}_2$ and $\text{Ga}_2\text{O}_3(300)\text{-H}_2$ is higher than that of the respective calcined catalysts by, respectively, 39, 23 and 38%. $\text{Ga}_2\text{O}_3(200)\text{-H}_2$ is the most active catalyst, yielding 193 and $56\text{ }\mu\text{mol C}_3\text{H}_6\text{ m}^{-2}\text{ h}^{-1}$ after 4 min and 104 min TOS, respectively, followed by $\text{Ga}_2\text{O}_3(250)\text{-H}_2$ (170 and $67\text{ }\mu\text{mol C}_3\text{H}_6\text{ m}^{-2}\text{ h}^{-1}$ after 4 min and 104 min TOS, respectively) and $\text{Ga}_2\text{O}_3(300)\text{-H}_2$ (155 and $68\text{ }\mu\text{mol}$

$\text{C}_3\text{H}_6\text{ m}^{-2}\text{ h}^{-1}$ after 4 min and 104 min TOS, respectively). $\text{Ga}_2\text{O}_3(200)\text{-H}_2$ deactivates the fastest, losing 71% of its initial activity after 104 min TOS, while $\text{Ga}_2\text{O}_3(250)\text{-H}_2$ and $\text{Ga}_2\text{O}_3(300)\text{-H}_2$ show similar deactivation rates, i.e. a loss of 61% and 56% over 104 min TOS, respectively. Initial propane conversions for these catalysts are ca. 27–30% (Table S4).

The initial propene selectivities are high and very similar among all of the six tested catalysts, i.e. in the range of 87–90% (Fig. 4B, Table S4). The decrease in propene selectivity with TOS is most pronounced for $\text{Ga}_2\text{O}_3(200)$, dropping from 88% after 4 min to 65% after 104 min. For comparison after 104 min TOS, the propene selectivities of $\text{Ga}_2\text{O}_3(250)$ and $\text{Ga}_2\text{O}_3(300)$ decline from 88% to 75% and from 90% to 77%, respectively. After 104 min TOS, the propene selectivities of $\text{Ga}_2\text{O}_3(250)\text{-H}_2$ and $\text{Ga}_2\text{O}_3(300)\text{-H}_2$ are 74% and 78%,

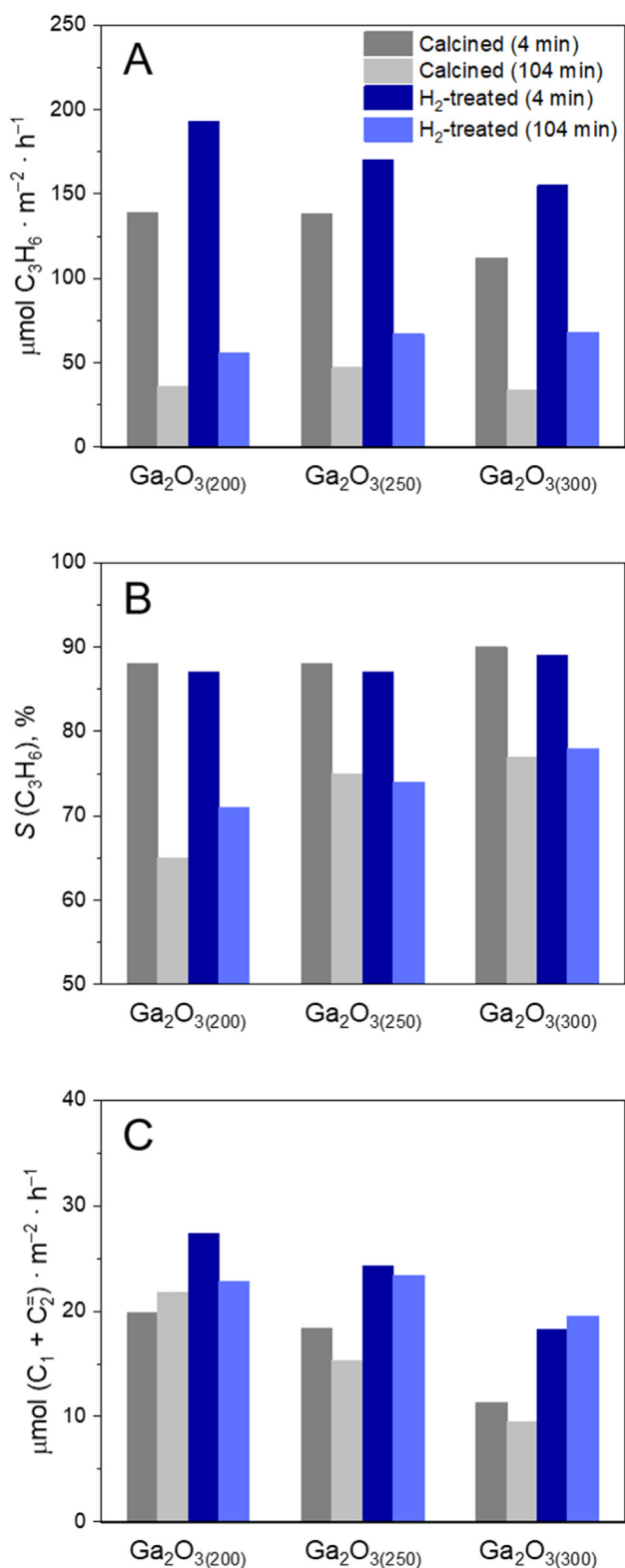


Fig. 4. Surface-area-normalized PDH activity (A), propene selectivity (B), and formation rates of cracking products (methane + ethene, (C)) of the calcined and H₂-treated Ga₂O₃ catalysts after 4 and 104 min of time on stream (see Figure S17 for details). WHSV = 9.5 h⁻¹, T = 550 °C.

that is, similar to the values of the respective calcined catalysts. After 104 min TOF, we observe only for Ga₂O₃₍₂₀₀₎-H₂ a higher selectivity (71%) relative to its calcined reference Ga₂O₃₍₂₀₀₎ (65%).

Turning now to the side reactions, the cracking rates to methane and ethene (Fig. 4C) are highest for Ga₂O₃₍₂₀₀₎ (19.8 and

21.8 μmol C₁ + C₂⁻ m⁻² h⁻¹ after 4 min and 104 min TOS respectively), followed by Ga₂O₃₍₂₅₀₎ (18.4 and 15.3 μmol C₁ + C₂⁻ h⁻¹ after 4 min and 104 min TOS respectively) and Ga₂O₃₍₃₀₀₎ (11.3 and 9.5 μmol C₁ + C₂⁻ m⁻² h⁻¹ after 4 min and 104 min TOS respectively). For all of the catalysts tested, H₂ treatment leads to an increase in the cracking rates, giving 27.4 and 22.8 μmol C₁ + C₂⁻ m⁻² h⁻¹ at 4 min and 104 min TOS for Ga₂O₃₍₂₀₀₎-H₂, 24.3 and 23.4 μmol C₁ + C₂⁻ m⁻² h⁻¹ at 4 min and 104 min TOS for Ga₂O₃₍₂₅₀₎-H₂ and 18.3 and 19.5 μmol C₁ + C₂⁻ h⁻¹ at 4 min and 104 min TOS for Ga₂O₃₍₃₀₀₎-H₂, respectively.

4. Discussion

In this work, we aimed to understand the effect of H₂ treatment on the local, periodic and defect structure, surface properties and catalytic PDH performance of three gallia catalysts that contain different ratios of γ-Ga₂O₃ and β-Ga₂O₃ polymorphs. Our recent DFT calculations using a structural model of β-Ga₂O₃ showed that Ga atoms in tetrahedral surface terminations and located next to V_o sites (i.e., Ga_{III} sites) feature weak LAS properties that likely drive PDH activity. [7] In light of these findings, the objectives of the present work were to understand how H₂ treatment modifies the local and periodic structure and the surface properties of Ga₂O₃ catalysts (LAS site distribution and strength), as well as how such changes at surface sites influence the catalysts' PDH activity.

Colloidal solutions of gallia NPs were prepared by varying the synthesis temperature and reaction time (200, 250 and 300 °C for 7, 12 and 16 h, respectively), yielding suspensions of ligand-capped γ-Ga₂O₃ nanoparticles. Calcination at 600 °C gave Ga₂O₃ NPs that contained different ratios of γ/β polymorphs; according to PDF analysis, the atomic fractions of β-Ga₂O₃ in Ga₂O₃₍₂₀₀₎, Ga₂O₃₍₂₅₀₎, and Ga₂O₃₍₃₀₀₎ were ca. 40%, 30% and 20% respectively.

H₂-treated Ga₂O₃ NPs were prepared by flowing hydrogen through a bed of calcined Ga₂O₃ NPs at 500 °C for 2 h. The H₂-treated materials were exposed to air after cooling down to room temperature. H₂ treatment did not lead to significant changes in the average (bulk) structure according to XRD and PDF analyses, yet it reduced the specific surface areas (by 26–36%) relative to the respective calcined materials (Table S5). The local structure of the Ga₂O₃ NPs was affected by H₂ treatment to various extents, as shown by the EXAFS analysis. We observed a decrease in the CN of the Ga–O and Ga–Ga shells of all H₂-treated catalysts, suggesting a more disordered local environment. After H₂ treatment, the lowest CN for the Ga–Ga shell were found in Ga₂O₃₍₃₀₀₎-H₂, indicating a higher degree of local disorder. It is possible that, due to a higher degree of mobility in the γ-rich nonstoichiometric spinel lattice, the gallium vacancies and the surface oxygen vacancies formed during H₂ treatment are directly reoccupied by atoms migrating from the core of the particle, thus leading to the formation of cationic vacancies and V_o sites in the bulk of the gallia nanoparticles. [51–53] In this context, previous H₂-TPR experiments in the literature had compared reducibility of unsupported α-, β-, γ- phases of Ga₂O₃ and found that while α-Ga₂O₃ and β-Ga₂O₃ lack reduction peaks, γ-Ga₂O₃ features a clear reduction peak centered at 344 °C, probably due to the formation of V_o sites. [54] Since the surface reduction of β-Ga₂O₃ forms V_o sites already above 277 °C, [55] it is likely that the observed higher reducibility of γ-Ga₂O₃ is linked to the formation of bulk V_o sites. Such an explanation is consistent with HAADF-STEM imaging that shows an increased degree of disorder in the sub-surface regions in Ga₂O₃₍₃₀₀₎-H₂ relative to Ga₂O₃₍₃₀₀₎. Yet the two outermost surface layers are highly ordered in both materials, in particular for Ga₂O₃₍₃₀₀₎-H₂. An additional piece of evidence for the increased local disorder in the bulk of Ga₂O₃₍₃₀₀₎-H₂ is provided by EELS that shows a broadening of the O K-edge peaks while the presence of a pre-edge feature suggested

the formation of new energy states (V_o) in the band gap of this material. Since γ -Ga₂O₃ contains a high density of structural defects, [56] it is likely that the migration of atoms (Ga, O) is favored in Ga₂O₃₍₃₀₀₎ relative to Ga₂O₃₍₂₀₀₎, which contains a larger fraction of the β -Ga₂O₃ phase.

The formation of V_o sites upon H₂ treatment is consistent with the UV–Vis results that revealed lower band gap energies for the H₂ treated materials (measured after exposure to atmospheric air), i.e. the band gap energies reduce from 4.1 to 4.3 eV in the calcined materials to 3.4–3.9 eV after H₂ treatment.

FTIR experiments reveal a sharp and intense Ga–OH band at ca. 3727 cm⁻¹ in Ga₂O₃₍₃₀₀₎ and, with a lower intensity, in Ga₂O₃₍₂₅₀₎. The band at 3727 cm⁻¹ is very weak in Ga₂O₃₍₂₀₀₎. Thus, for the series of materials studied here the intensity of the hydroxyl band at 3727 cm⁻¹ correlates directly with the fraction of the γ -Ga₂O₃ phase present in the Ga₂O₃ NPs. Hydroxyl bands of similar shape and position have been observed in defective spinels (such as γ -Al₂O₃ or γ -Ga₂O₃). Previous works have associated hydroxyl bands at such high wavenumbers with crystallographic cation defect sites while broader bands at lower wavenumbers have been related to Ga–OH sites on terraces. [41,43].

Surface hydrides form three Ga–H bands in Ga₂O₃₍₂₀₀₎-H₂ and Ga₂O₃₍₂₅₀₎-H₂, however, the lower frequency band (at ca. 1931–1939 cm⁻¹ due to weaker Ga–H bonds) is missing in Ga₂O₃₍₃₀₀₎-H₂. Our DFT calculations on model dehydroxylated β -Ga₂O₃ surfaces did not allow for an unequivocal assignment of the Ga geometry for each of these Ga–H sites. Nonetheless, Ga_v-H sites show higher vibrational frequencies than Ga_{III}-H sites. That being said, there is a correlation between the higher relative abundance of the low-frequency Ga hydride bands in two of the studied Ga₂O₃-H₂ materials with the higher relative abundance of weak LAS, the higher relative fraction of β -Ga₂O₃ and the higher catalytic activity displayed by these materials, which suggests that the low-frequency Ga–H band at ca. 1931–1939 cm⁻¹ may be assigned to Ga_{III}-H sites. In other words, weak LAS form the low-frequency Ga hydride bands associated with weaker Ga–H bonds and such sites are likely connected to faster site regeneration due to easier H₂ desorption. However, other studies have suggested that the presence of V_o leads to strongly bonded hydrides, presumably on Ga_{CUS} sites. [55]

¹⁵N DNP SENS results reveal differences between the relative fractions of weak, mild and strong LAS in the studied catalysts. Among the calcined materials, weak LAS are most abundant in Ga₂O₃₍₂₀₀₎, less abundant (but detectable) in Ga₂O₃₍₂₅₀₎ and lacking in Ga₂O₃₍₃₀₀₎. This trend parallels the relative amount of the β -Ga₂O₃ phase in those materials; that is, predominantly γ -phase Ga₂O₃₍₃₀₀₎ contains no weak LAS. In our recent work, we have associated weak LAS in β -Ga₂O₃ with tricoordinated Ga sites (Ga_{III}), i.e. Ga atoms in a tetrahedral position located next to a V_o site. [7] In this context, it is interesting to note that despite the presence of abundant V_o sites, the surface of Ga₂O₃₍₃₀₀₎-H₂ lacks Ga_{III} sites since Ga₂O₃₍₃₀₀₎-H₂ contains no weak LAS, which is in agreement with the absence of low-frequency Ga–H moieties in the FTIR spectrum (*vide supra*). Moreover, while we observe a strong increase of the number of weak LAS after H₂ treatment in Ga₂O₃₍₂₀₀₎-H₂ (nearly by a factor of 4, up to 27%), explained by the formation of surface V_o sites in the β -Ga₂O₃ phase that is present in Ga₂O₃₍₂₀₀₎-H₂, the opposite effect is observed in Ga₂O₃₍₃₀₀₎-H₂, for which the relative fraction of strong LAS nearly doubles relative to Ga₂O₃₍₃₀₀₎, reaching 57%, while no weak LAS were detected. The higher density of strong LAS in the surface of Ga₂O₃₍₃₀₀₎-H₂ can be related to the increased occupancy of Ga_{VI} positions in the surface layers relative to Ga₂O₃₍₃₀₀₎, as evidenced by HAADF-STEM. The presence of Ga in octahedral surface termination positions has been linked previously to strong LAS. [7,8].

Interestingly, while the fitting of the PDF data shows atomic percentages of β -Ga₂O₃ of ca. 40%, 30% and 20% for Ga₂O₃₍₂₀₀₎, Ga₂O₃₍₂₅₀₎ and Ga₂O₃₍₃₀₀₎, respectively, results of ¹⁵N DNP SENS show the lack of weak LAS, typical of β -Ga₂O₃, on the surface of Ga₂O₃₍₃₀₀₎. This result may be interpreted as an indication that the core of Ga₂O₃₍₃₀₀₎ has an atomic structure resembling β -Ga₂O₃ while the shell (surface) retains the structure of γ -Ga₂O₃.

Finally, we relate the evolution of LAS during H₂ treatment to changes in the catalytic activity in PDH. The increase of the initial activity of materials that contain the highest fraction of β -Ga₂O₃ upon hydrogen treatment, i.e. Ga₂O₃₍₂₀₀₎-H₂ and, to a lesser extent, Ga₂O₃₍₂₅₀₎-H₂, can be explained by an increase in the relative density of weak LAS, especially in Ga₂O₃₍₂₀₀₎-H₂ that also features a decreased fraction of strong LAS, which may explain the more stable propene selectivity of the H₂ treated NPs. γ -Rich Ga₂O₃₍₃₀₀₎ also increases its initial activity after H₂ treatment, despite the fact that Ga₂O₃₍₃₀₀₎-H₂ lacks weak LAS and features an increased fraction of less active and more quickly deactivating strong LAS. A possible explanation for this result is the higher density of surface Ga sites in Ga₂O₃₍₃₀₀₎-H₂ relative to Ga₂O₃₍₃₀₀₎, i.e. surface reconstruction as a result of H₂ treatment takes place in Ga₂O₃₍₃₀₀₎-H₂ and this disorders the core of Ga₂O₃₍₃₀₀₎-H₂ (decreasing coordination numbers of Ga–O and Ga–Ga coordination shells) and densifies the two outer layers (higher density of Ga sites in HAADF STEM line intensity profiles). Lastly, the more defective surfaces in Ga₂O₃₍₂₀₀₎ and Ga₂O₃₍₂₅₀₎, either calcined or H₂-treated, produce higher amounts of cracking products relative to the less defective surfaces in Ga₂O₃₍₃₀₀₎ and Ga₂O₃₍₃₀₀₎-H₂.

5. Conclusions

In conclusion, we report that the material with the highest fraction of β -Ga₂O₃ is more active in PDH than the γ -rich Ga₂O₃ catalyst due to the higher proportion of weak LAS in β -Ga₂O₃; our results show that γ -Ga₂O₃ lacks these sites. Such weak LAS are likely Ga_{CUS} (i.e. Ga_{III}) sites. H₂ treatment of catalysts at 500 °C creates additional V_o sites in both γ -Ga₂O₃ and β -Ga₂O₃. The surface of β -rich Ga₂O₃ can accommodate V_o sites, and this creates more Ga_{CUS}, which in turn increases both the fraction of weak LAS and PDH activity. In contrast, no weak LAS are generated when treating the γ -rich Ga₂O₃ in H₂, despite the presence of abundant V_o sites in the bulk of the H₂ treated material. However, as we observe a doubling of the fraction of strong LAS (due to an increased relative amount of surface Ga sites in octahedral surface termination positions) and an increased density of Ga sites in the two outermost layers in γ -rich Ga₂O₃, it is likely that a surface reconstruction has occurred during the H₂ treatment of this material. Therefore, the higher activity in γ -rich Ga₂O₃ after H₂ treatment is explained by an increased density of surface Ga sites.

Funding Sources

We acknowledge funding from the European Research Council (ERC) under the European Union's Horizon 2020 research and innovation program (grant agreement No. 819573), from the Swiss National Science Foundation (IZSEZO_178677) and from ETH Postdoctoral Fellowship Program and the Marie Curie Actions for People COFUND (grant no. 18–1 FEL 51).

Declaration of Competing Interest

The authors declare that they have no known competing financial interests or personal relationships that could have appeared to influence the work reported in this paper.

Acknowledgement

We thank the Scientific Centre for Optical and Electron Microscopy (ScopeM) of ETH Zürich for providing access to electron microscopes. The Swiss Norwegian beamlines (SNBL, ESRF) are acknowledged for provision of beamtime through proposal CH31-0133. Dr. Wouter van Beek and Dr. Dragos Stoian (SNBL, ESRF) are acknowledged for their support during the XAS experiments. We would also like to thank Dr. Agnieszka Kierzkowska (ETH Zürich) for carrying out ICP-OES measurements.

Author Contributions

P.C.-F. and A.F. conceived the research project and designed experiments. P.C.-F. synthesized and characterized materials and analysed data. D.M. conducted ^{15}N DNP SENS experiments. C.L. and E.A.P. performed and interpreted DFT modelling. P.M.A. supervised XAS experiments and data analysis. E.W. performed and analysed HAADF-STEM and EELS experiments. A.R. analysed part of the data. A.I.S. carried out H_2 -FTIR experiments and supervised data analysis. Data were discussed among all co-authors. P.C.-F. and A.F. wrote the first draft that was reviewed and edited by all authors. All authors gave their final approval to the final version of the manuscript.

Appendix A. Supplementary data

Supporting Information for this article contains experimental methods, TEM images, Tauc plots, XRD, PDF, XAS, EELS, FTIR, computational data and catalytic tests. Supplementary data to this article can be found online at <https://doi.org/10.1016/j.jcat.2022.02.025>.

References

- J.J.H.B. Sattler, J. Ruiz-Martinez, E. Santillan-Jimenez, B.M. Weckhuysen, Catalytic Dehydrogenation of Light Alkanes on Metals and Metal Oxides, *Chem. Rev.* 114 (2014) 10613–10653.
- S. Chen, X. Chang, G. Sun, T. Zhang, Y. Xu, Y. Wang, C. Pei, J. Gong, Propane Dehydrogenation: Catalyst Development, New Chemistry, and Emerging Technologies, *Chem. Soc. Rev.* 50 (2021) 3315–3354.
- J.J.H.B. Sattler, I.D. Gonzalez-Jimenez, L. Luo, B.A. Stears, A. Malek, D.G. Barton, B.A. Kilos, M.P. Kaminsky, T.W.G.M. Verhoeven, E.J. Koers, et al., Platinum-Promoted Ga/Al₂O₃ as Highly Active, Selective, and Stable Catalyst for the Dehydrogenation of Propane, *Angew. Chem. Int. Ed.* 53 (2014) 9251–9256.
- P.-A. Payard, L. Rochlitz, K. Searles, L. Foppa, B. Leuthold, O.V. Safonova, A. Comas-Vives, C. Copéret, Dynamics and Site Isolation: Keys to High Propane Dehydrogenation Performance of Silica-Supported PtGa Nanoparticles, *JACS Au* 1 (2021) 1445–1458.
- N. Raman, M. Wolf, M. Heller, N. Heene-Würl, N. Taccardi, M. Haumann, P. Felfel, P. Wasserscheid, GaPt Supported Catalytically Active Liquid Metal Solution Catalysis for Propane Dehydrogenation-Support Influence and Coking Studies, *ACS Catal.* 11 (21) (2021) 13423–13433.
- K. Searles, K.W. Chan, J.A. Mendes Burak, D. Zemlyanov, O. Safonova, C. Copéret, Highly Productive Propane Dehydrogenation Catalyst Using Silica-Supported Ga-Pt Nanoparticles Generated from Single-Sites, *J. Am. Chem. Soc.* 140 (37) (2018) 11674–11679.
- P. Castro-Fernández, D. Mance, C. Liu, I.B. Moroz, P.M. Abdala, E.A. Pidko, C. Copéret, A. Fedorov, C.R. Müller, Propane Dehydrogenation on Ga₂O₃-Based Catalysts: Contrasting Performance with Coordination Environment and Acidity of Surface Sites, *ACS Catal.* 11 (2021) 907–924.
- P. Castro-Fernández, M. Kaushik, Z. Wang, D. Mance, E. Kountoupi, E. Willinger, P.M. Abdala, C. Copéret, A. Lesage, A. Fedorov, et al., Uncovering Selective and Active Ga Surface Sites in Gallia-Alumina Mixed-Oxide Propane Dehydrogenation Catalysts by Dynamic Nuclear Polarization Surface Enhanced NMR Spectroscopy, *Chem. Sci.* 12 (2021) 15273–15283.
- E.A. Pidko, R.A. Van Santen, Structure-Reactivity Relationship for Catalytic Activity of Gallium Oxide and Sulfide Clusters in Zeolite, *J. Phys. Chem. C* 113 (2009) 4246–4249.
- E.A. Pidko, R.A. Van Santen, E.J.M. Hensen, Multinuclear Gallium-Oxide Cations in High-Silica Zeolites, *Phys. Chem. Chem. Phys.* 11 (2009) 2893–2902.
- Z. Xie, Z. Li, P. Tang, Y. Song, Z. Zhao, L. Kong, X. Fan, X. Xiao, The Effect of Oxygen Vacancies on the Coordinatively Unsaturated Al-O Acid-Base Pairs for Propane Dehydrogenation, *J. Catal.* 397 (2021) 172–182.
- D. Zhao, H. Lund, U. Rodemerck, D. Linke, G. Jiang, E.V. Kondratenko, Revealing Fundamentals Affecting Activity and Product Selectivity in Non-Oxidative Propane Dehydrogenation over Bare Al₂O₃, *Catal. Sci. Technol.* 11 (2021) 1386–1394.
- C.-F. Li, X. Guo, Q.-H. Shang, X.i. Yan, C. Ren, W.-Z. Lang, Y.-J. Guo, Defective TiO₂ for Propane Dehydrogenation, *Ind. Eng. Chem. Res.* 59 (10) (2020) 4377–4387.
- Z. Xie, T. Yu, W. Song, J. Li, Z. Zhao, B. Liu, Z. Gao, D. Li, Highly Active Nanosized Anatase TiO_{2-x} Oxide Catalysts In Situ Formed through Reduction and Ostwald Ripening Processes for Propane Dehydrogenation, *ACS Catal.* 10 (2020) 14678–14693.
- Y. Zhang, Y. Zhao, T. Otroshchenko, H. Lund, M.M. Pohl, U. Rodemerck, D. Linke, H. Jiao, G. Jiang, E.V. Kondratenko, Control of Coordinatively Unsaturated Zr Sites in ZrO₂ for Efficient C-H Bond Activation, *Nat. Commun.* 9 (2018) 3794.
- T. Otroshchenko, S. Sokolov, M. Stoyanova, V.A. Kondratenko, U. Rodemerck, D. Linke, E.V. Kondratenko, ZrO₂-Based Alternatives to Conventional Propane Dehydrogenation Catalysts: Active Sites, Design, and Performance, *Angew. Chem. - Int. Ed.* 54 (2015) 15880–15883.
- Y. Yun, J.R. Araujo, G. Melaet, J. Baek, B.S. Archanjo, M. Oh, A.P. Alivisatos, G.A. Somorjai, Activation of Tungsten Oxide for Propane Dehydrogenation and Its High Catalytic Activity and Selectivity, *Catal. Letters* 147 (2017) 622–632.
- G.S. Parkinson, Iron Oxide Surfaces, *Surf. Sci. Rep.* 71 (2016) 272–365.
- Y. Li, L. Lin, L. Gao, R. Mu, Q. Fu, X. Bao, Predominance of Subsurface and Bulk Oxygen Vacancies in Reduced Manganese Oxide, *J. Phys. Chem. C* 125 (2021) 7990–7998.
- A.J. Rossini, A. Zagdoun, M. Lelli, A. Lesage, C. Copéret, L. Emsley, Dynamic Nuclear Polarization Surface Enhanced NMR Spectroscopy, *Acc. Chem. Res.* 46 (2013) 1942–1951.
- T. Kobayashi, F.A. Perras, I.I. Slowing, A.D. Sadow, M. Pruski, Dynamic Nuclear Polarization Solid-State NMR in Heterogeneous Catalysis Research, *ACS Catal.* 5 (2015) 7055–7062.
- T. Wang, S.S. Farvid, M. Abulikemu, P.V. Radovanovic, Size-Tunable Phosphorescence in Colloidal Metastable γ -Ga₂O₃ Nanocrystals, *J. Am. Chem. Soc.* 132 (2010) 9250–9252.
- P. Castro-Fernández, M.V. Blanco, R. Verel, E. Willinger, A. Fedorov, P.M. Abdala, C.R. Müller, Atomic-Scale Insight into the Structure of Metastable γ -Ga₂O₃ Nanocrystals and Their Thermally-Driven Transformation to β -Ga₂O₃, *J. Phys. Chem. C* 124 (2020) 20578–20588.
- J. Tauc, Optical Properties and Electronic Structure of Amorphous Ge and Si, *Mater. Res. Bull.* 3 (1968) 37–46.
- A. Dolgonos, S.A. Wells, K.R. Poeppelmeier, T.O. Mason, Phase Stability and Optoelectronic Properties of the Bixbyite Phase in the Gallium-Indium-Tin-Oxide System, *J. Am. Ceram. Soc.* 98 (2014) 669–674.
- T. Chen, K. Tang, γ -Ga₂O₃ Quantum Dots with Visible Blue-Green Light Emission Property, *Appl. Phys. Lett.* 90 (2007) 3–6.
- M. Orita, O. Hirouchi, M. Hirano, H. Hosono, Deep-Ultraviolet Transparent Conductive B-Ga₂O₃ Thin Films, *Appl. Phys. Lett.* 4166 (2000) 4166–4168.
- P.R. Jubu, F.K. Yam, A.T. Moses, Deposition of Gallium Oxide Nanostructures at Low Substrate Temperature by Chemical Vapor Deposition, *ECS J. Solid State Sci. Technol.* 9 (2020) 035006.
- H. Liu, F. Zeng, Y. Lin, G. Wang, F. Pan, Correlation of Oxygen Vacancy Variations to Band Gap Changes in Epitaxial ZnO Thin Films, *Appl. Phys. Lett.* 102 (18) (2013) 181908.
- P.S. Vachhani, A.K. Bhatnagar, Oxygen Pressure-Dependent Band Gap Modification in Cu-Doped and -Undoped ZnO Films, *Phys. Scr.* 87 (4) (2013) 045702.
- X. Zhang, Z. Zhang, H. Huang, Y. Wang, N. Tong, J. Lin, D. Liu, X. Wang, Oxygen Vacancy Modulation of Two-Dimensional γ -Ga₂O₃ Nanosheets as Efficient Catalysts for Photocatalytic Hydrogen Evolution, *Nanoscale* 10 (2018) 21509–21517.
- J. Wang, Z. Wang, B. Huang, Y. Ma, Y. Liu, X. Qin, X. Zhang, Y. Dai, Oxygen Vacancy Induced Band-Gap Narrowing and Enhanced Visible Light Photocatalytic Activity of ZnO, *ACS Appl. Mater. Interfaces* 4 (2012) 4024–4030.
- M. Zinkevich, F.M. Morales, H. Nitsche, M. Ahrens, M. Rühle, F. Aldinger, Microstructural and Thermodynamic Study of γ -Ga₂O₃, *Z. Met.* 95 (2004) 756–762.
- M.A.F.M. da Silva, L.P. Sosman, F. Yokaichiya, V.L. Mazzocchi, C.B.R. Parence, J. Mestnik-Filho, P.F. Henry, H.N. Bordallo, Neutron Powder Diffraction Measurements of the Spinel MgGa₂O₄:Cr³⁺ - A Comparative Study between the High Flux Diffractometer D2B at the ILL and the High Resolution Powder Diffractometer Aurora at IPEN, *J. Phys. Conf. Ser.* 340 (2012) 012041.
- H.Y. Playford, A.C. Hannon, M.G. Tucker, D.M. Dawson, S.E. Ashbrook, R.J. Kastiban, J. Sloan, R.I. Walton, Characterization of Structural Disorder in γ -Ga₂O₃, *J. Phys. Chem. C* 118 (2014) 16188–16198.
- K. Nishi, K. Shimizu, M. Takamatsu, H. Yoshida, A. Satsuma, T. Tanaka, S. Yoshida, T. Hattori, Deconvolution Analysis of Ga K-Edge XANES for Quantification of Gallium Coordinations in Oxide Environments, *J. Phys. Chem. B* 102 (1998) 10190–10195.
- A. Sharma, M. Varshney, H. Shin, K.H. Chae, S.O. Won, Investigation on Cation Distribution and Luminescence in Spinel Phase γ -Ga_{3-x}O₄:Sm Nanostructures Using X-Ray Absorption Spectroscopy, *RSC Adv.* 7 (2017) 52543–52554.
- X.T. Zhou, F. Heigl, J.Y.P. Ko, M.W. Murphy, J.G. Zhou, T. Regier, R.I.R. Blyth, T.K. Sham, Origin of Luminescence from Ga₂O₃ Nanostructures Studied Using X-Ray Absorption and Luminescence Spectroscopy, *Phys. Rev. B* 75 (2007) 125303.

- [39] S.E. Collins, M.A. Baltanás, A.L. Bonivardi, Hydrogen Chemisorption on Gallium Oxide Polymorphs, *Langmuir* 21 (2005) 962–970.
- [40] C. Copéret, D.P. Estes, K. Larmier, K. Searles, Isolated Surface Hydrides: Formation, Structure, and Reactivity, *Chem. Rev.* 116 (2016) 8463–8505.
- [41] S.D. Jackson, J.S.J. Hargreaves, *Metal Oxide Catalysis*, 2009th ed.; WILEY-VCH Verlag GmbH & Co., KGaA, Weinheim: Weinheim, 2009.
- [42] S.E. Collins, M.A. Baltanás, A.L. Bonivardi, Infrared Spectroscopic Study of the Carbon Dioxide Adsorption on the Surface of Ga₂O₃ Polymorphs, *J. Phys. Chem. B* 110 (2006) 5498–5507.
- [43] A. Vimont, J.C. Lavalley, A. Sahibed-Dine, C. Otero-Areán, M. Rodríguez Delgado, M. Daturi, C. Otero Arean, M. Rodríguez Delgado, M. Daturi, Infrared Spectroscopic Study on the Surface Properties of Gamma-Gallium Oxide as Compared to Those of Gamma-Alumina, *J. Phys. Chem. B* 109 (2005) 9656–9664.
- [44] S.E. Collins, M.A. Baltanás, J.L. García-Fierro, A.L. Bonivardi, Gallium-Hydrogen Bond Formation on Gallium and Gallium-Palladium Silica-Supported Catalysts, *J. Catal.* 211 (2002) 252–264.
- [45] E.A. Gonzalez, P.V. Jasen, A. Juan, S.E. Collins, M.A. Baltanás, A.L. Bonivardi, Hydrogen Adsorption on β -Ga₂O₃(100) Surface Containing Oxygen Vacancies, *Surf. Sci.* 575 (2005) 171–180.
- [46] J. Vecchietti, M.A. Baltanás, C. Gervais, S.E. Collins, G. Blanco, O. Matz, M. Calatayud, A. Bonivardi, Insights on Hydride Formation over Cerium-Gallium Mixed Oxides: A Mechanistic Study for Efficient H₂ Dissociation, *J. Catal.* 345 (2017) 258–269.
- [47] D. Michel, A. Germanus, H. Pfeifer, Nitrogen-15 Nuclear Magnetic Resonance Spectroscopy of Adsorbed Molecules, *J. Chem. Soc. Faraday Trans. 78* (1982) 237.
- [48] T. Bernstein, L. Kitaev, M. Dieter, H. Pfeifer, Carbon-13 and Nitrogen-15 Nuclear Magnetic Resonance and Infrared Spectroscopic Investigations of Pyridine Adsorbed on Silica-Gel Surfaces, *J. Chem. Soc., Faraday Trans. 78* (1982) 761–769.
- [49] W.R. Gunther, V.K. Michaelis, R.G. Griffin, Y. Roman-Leshkov, Interrogating the Lewis Acidity of Metal Sites in Beta Zeolites with ¹⁵N Pyridine Adsorption Coupled with MAS NMR Spectroscopy, *J. Phys. Chem. C* 120 (2016) 28533–28544.
- [50] I.B. Moroz, K. Larmier, W.-C. Liao, C. Copéret, Discerning γ -Alumina Surface Sites with Nitrogen-15 Dynamic Nuclear Polarization Surface Enhanced NMR Spectroscopy of Adsorbed Pyridine, *J. Phys. Chem. C* 122 (2018) 10871–10882.
- [51] D.B. Buchholz, Q. Ma, D. Alducin, A. Ponce, M. Jose-Yacaman, R. Khanal, J.E. Medvedeva, R.P.H. Chang, The Structure and Properties of Amorphous Indium Oxide, 26 (18) (2014) 5401–5411.
- [52] A. Tsoukalou, P.M. Abdala, D. Stoian, X. Huang, M.G. Willinger, A. Fedorov, C.R. Müller, Structural Evolution and Dynamics of an In₂O₃ Catalyst for CO₂ Hydrogenation to Methanol: An Operando XAS-XRD and in Situ TEM Study, *J. Am. Chem. Soc.* 141 (2019) 13497–13505.
- [53] S.C. Siah, S.W. Lee, Y.S. Lee, J. Heo, T. Shibata, C.U. Segre, R.G. Gordon, T. Buonassisi, X-Ray Absorption Spectroscopy Elucidates the Impact of Structural Disorder on Electron Mobility in Amorphous Zinc-Tin-Oxide Thin Films, *Appl. Phys. Lett.* 104 (24) (2014) 242113.
- [54] L. Li, W. Wei, M. Behrens, Synthesis and Characterization of α -, β -, and γ -Ga₂O₃ Prepared from Aqueous Solutions by Controlled Precipitation, *Solid State Sci.* 14 (2012) 971–981.
- [55] W. Jochum, S. Penner, K. Föttinger, R. Kramer, G. Rupprechter, B. Klötzer, Hydrogen on Polycrystalline β -Ga₂O₃: Surface Chemisorption, Defect Formation, and Reactivity, *J. Catal.* 256 (2008) 268–277.
- [56] K. Pohl, Hydrothermal Formation of γ -Ga₂O₃, *Naturwissenschaften* 55 (1968) 82.